Anisotropic Straintronic Transport in Topological Semimetal Nanoflakes

Tongxie Zhang<sup>1+</sup>, Jeonghoon Hong<sup>1+</sup>, Amanda L. Coughlin<sup>1</sup>, Cynthia Nnokwe<sup>2</sup>, Michael K.

Hosek<sup>1</sup>, Rui He<sup>2</sup>, Herbert A. Fertig<sup>1,3</sup>, Shixiong Zhang<sup>1,3\*</sup>

1. Department of Physics, Indiana University, Bloomington, Indiana 47405, United States

2. Department of Electrical and Computer Engineering, Texas Tech University, Lubbock, Texas

79409, United States

3. Quantum Science and Engineering Center, Indiana University, Bloomington, Indiana 47405,

**United States** 

+ These two authors contributed equally.

\*Email: sxzhang@indiana.edu

**ABSTRACT** 

Strain engineering is not only a powerful tool to enhance the functional properties of quantum

materials for practical applications but also a unique technique to uncover the underlying

mechanisms dictating those properties. One of the most promising systems for strain engineering

is the two-dimensional materials, such as transition metal dichalcogenide (TMD) thin layers,

which have large mechanical strength and highly sensitive electronic and optical properties. Most

of the previous experimental studies have focused on semiconducting TMDs by tuning their

bandgap and electrical properties at room temperature. Here we report for the first time low-

temperature, strain-dependent magneto-transport studies of semimetal WTe<sub>2</sub> nanoflake devices.

By applying a uniaxial tensile strain along two crystallographic directions (a- and b- axes), we

have observed a clear anisotropic elastoresistivity, where the resistivity has opposite responses to

1

the applied strain in the two directions. The electron density extracted from the magnetoresistance and Hall measurements decreases as a function of tensile strain along the a-axis and increases

along the b-axis. The anisotropic strain-dependence of transport properties are understood based

on the density functional theory calculations of the electronic band structures and Fermi surfaces.

Our work experimentally demonstrates strain as an effective tool to tune the low-temperature

transport properties of nanostructured topological metals for straintronic applications.

**KEYWORDS:** strain, magneto-transport, semimetal, two-dimensional materials, WTe<sub>2</sub>

1. Introduction

The electronic band structure of a solid-state material is dictated by its crystal lattice structure.

Applying mechanical stress or pressure to a material induces strain (or deformation of the lattice

structure) which modifies its electronic structure and subsequently tunes its associated physical

properties. Such strain-electronic (or straintronic) engineering is not only a powerful technique to

enhance the functional properties of materials for electronic applications or achieve exotic states

that are not intrinsically present in a material, but can also provide important insight into the

underlying mechanisms of its fundamental properties. Indeed, strain has been widely utilized to

improve the performance of silicon-based metal oxide semiconductor field-effect transistors

(MOSFETs) in modern electronics. 1 It has also been demonstrated to increase the superconducting

transition temperature  $T_{c,2}$  induce new magnetic phases,<sup>3</sup> control valley-dependent charge

transport,<sup>4</sup> and probe exotic nematic electronic order<sup>5-7</sup> in a variety of bulk single crystals.

Compared with bulk crystals, two-dimensional (2D) van der Waals (vdW) nanomaterials, such

as graphene and transition metal dichalcogenides (TMDs), can withstand significantly higher

strains before fracturing, offering an excellent platform for strain engineering of electronic and

2

optical properties.<sup>8-15</sup> A variety of intriguing responses to strain have been experimentally observed in 2D vdW semiconductors at room temperature.<sup>16-23</sup> For example, uniaxial tensile strain realized by a bending method has been reported to reduce the bandgap in monolayer and bilayer MoS<sub>2</sub>,<sup>16</sup> and to double the mobility in monolayer MoS<sub>2</sub>.<sup>21</sup> Tensile strain, induced by either bending or elongating, also gives rise to direct-indirect and indirect-direct bandgap transitions in monolayer WS<sub>2</sub> and bilayer WSe<sub>2</sub>, respectively.<sup>18, 19</sup> Using a piezoelectric strain cell, a reversible strain-induced antiferromagnetic-to-ferromagnetic phase transition was realized in CrSBr flakes.<sup>23</sup> As such, strain has great potential to enhance the performance of 2D semiconductor-based electronic, optoelectronic and spintronic devices.

Less attention, however, has been paid to metallic or semimetallic TMDs which typically possess intriguing electrical transport properties at low temperatures. As a prominent example, the semimetal WTe<sub>2</sub> exhibits an extremely large (~452,700%) and non-saturating magnetoresistance (MR) at 4.5 K and 14.7 T, due to nearly compensated electron and hole pockets in its band structure.<sup>24</sup> This extremely large MR provides WTe<sub>2</sub> with potential applications in magnetic sensors or magnetic memory devices.<sup>25</sup> To study how the intriguing electrical properties of WTe<sub>2</sub> are influenced by strain, an *in situ* strain-transport measurement apparatus that can be operated at low temperatures and high magnetic fields is required. Due to this technical challenge, there are only limited transport studies on strain effects in WTe<sub>2</sub>,<sup>26</sup> in spite of numerous theoretical predictions based on first-principles calculations.<sup>26-31</sup> A single experimental study<sup>26</sup> focused on bulk single crystal samples, where a large magnetoelastoresistance (MER) was observed under a uniaxial *compressive* strain along the *a*-axis of the WTe<sub>2</sub> lattice. The bulk crystals, however, were only able to tolerate up to -0.16% compressive strain before fracturing. While first-principles and analytical low-energy model calculations suggest a dominating role of the strain-tuned charge

carrier densities in its MER, direct experimental measurements are lacking. Furthermore, given the highly anisotropic and temperature-sensitive electronic structure of WTe<sub>2</sub>,<sup>24, 32-38</sup> it is also crucial to explore the effects of strain on electrical transport along different crystallographic axes at various temperatures.

Here we report a study of anisotropic strain effects on the magneto-transport properties of WTe<sub>2</sub> nanoflake devices up to +0.56% *tensile* strain, using a three-point bending apparatus which allows for strain-magneto-transport measurements down to 4 K and up to 7 Tesla. We focus on thin nanoflakes as they presumably have few stacking faults, and hence can withstand higher strains compared to their bulk counterparts.<sup>39, 40</sup> Beyond demonstrating a controllable and reversible tuning of resistance by strain, MR and Hall resistivity ( $\rho_{xy}$ ) were measured under the application of a uniaxial *tensile* strain along both the a and b axes, enabling the determination of strain-dependent charge carrier densities and mobilities. A large anisotropy effect is observed between the two directions, which we understand semi-quantitatively using first-principles density functional theory (DFT) calculations. Our work experimentally demonstrates strain as an effective knob to tune the low-temperature magneto-transport properties of nanostructured topological metals for straintronic applications.

# 2. Experimental and Calculation Details

2.1 Device Fabrication: Cr/Au (10 nm/90 nm) pads were deposited onto a pristine flexible SiO<sub>2</sub>/Si (300 nm/50 $\mu$ m) substrate through optical lithography and thermal evaporation processes. The SiO<sub>2</sub>/Si substrate was securely affixed to a non-magnetic beryllium copper sheet with cryogenic epoxy. WTe<sub>2</sub> nanoflakes were exfoliated from a bulk crystal (purchased from 2D semiconductors) and mechanically transferred to the center of the substrate using polydimethylsiloxane (PDMS).

Cr/Au (10 nm/200 nm) electrodes were fabricated through electron beam lithography and thermal evaporation; these electrodes connect the nanoflakes to the prefabricated Cr/Au pads for subsequent transport measurements. The large electrode thickness was to prevent any potential slippage of the nanoflakes. <sup>16, 41</sup> Plasma cleaning and HCl etching were conducted before metal evaporation to remove any possible organic materials and surface oxides. The total thickness t measured from the top of the device chip to the bottom of the BeCu sheet was ~200 ±10  $\mu$ m. The thickness of each nanoflake was characterized via atomic force microscopy. A schematic picture and a photograph of a flexible device are shown in Fig. 1 (a) and (b), respectively.

2.2 Resistivity and Magneto-transport Measurements: Resistivity and magneto-transport measurements were conducted using a partially home-built system, which incorporated the Quantum Design Magnetic Property Measurement System (MPMS). The measured device was securely fixed onto the end of a long hollow sample rod and was wire-bonded to wires which were fed through the center of the sample rod to connect to a Linear Research 700 (LR-700) AC Resistance Bridge. The longitudinal resistance and Hall resistance of the nanoflakes were measured in typical four-terminal and Hall configurations with the magnetic field applied perpendicular to the nanoflake (along the *c* axis). Antisymmetric Hall resistance signal was subtracted from the magnetoresistance measurements, and symmetric magnetoresistance signal was subtracted from the Hall resistance measurements. The MPMS software was used to set and read both the temperature and magnetic field, and these values were recorded in the same data file that captured the resistance measurements. Both longitudinal resistance and Hall resistance values were averaged at each magnetic field point after the field stabilized at the setpoint. All To apply uniaxial tensile strain via a three-point bending method (Figure 1b), a thinner rod was inserted

through the sample rod to push the flexible device and its position was measured by a built-in micrometer screw gauge.

2.3 Computational Methods: DFT calculations were carried out using the projected augmented plane-wave (PAW) method,  $^{44, 45}$  as implemented in the Vienna Ab Initio Simulation Package (VASP),  $^{46}$  For the exchange-correlation interactions among electrons, we employed the Perdew-Burke-Ernzerhof (PBE) generalized gradient approximation (GGA). The convergence criteria for the atomic forces were set to be less than 0.001 eV Å $^{-1}$  and that for the total energy to be  $10^{-6}$  eV. To sample the Brillouin zone, a dense  $12 \times 6 \times 3$  k-point grid was used. Spin-orbit coupling has been included in the calculations. Additionally, the WANNIER90 code $^{47}$  was leveraged to construct a tight-binding Hamiltonian, and the Fermi surface was determined using a  $1000 \times 1000 \times 1$  k-point grid. The electron or hole carrier density in an ellipsoidal Fermi surface was determined by aggregating the areas of multiple slices to estimate the volume of each pocket. This volume was then normalized by the Brillouin zone volume, directly correlating the ellipsoidal volumes with the carrier density.  $^{48, 49}$ 

#### 3. Results and Discussions

As illustrated in Figure 1c, WTe<sub>2</sub> layers stack along the c-axis, and within each monolayer, one-dimensional zigzag chains of W atoms are formed along the a-axis due to the distortion in the T<sub>d</sub> structure. These atomic chains are separated by a relatively large distance along the b-axis.<sup>50</sup> Uniaxial tensile strain was applied to the nanoflakes along either a or b axis via a bending method, <sup>16, 18, 20, 21, 51, 52</sup> as described in Section 2.2. The magnitude of the strain was controlled by bending the BeCu sheet via pushing it away from its neutral position a certain distance, and is described by the equation  $\varepsilon = t/(2r)$ , <sup>52</sup> where t is the total thickness measured from the top of the device chip to the bottom of the BeCu sheet, and r is the radius of curvature of the bent device

(Section 1 in the Supporting Information). Since the thicknesses of the nanoflakes (tens of nanometers) are significantly smaller than t (200  $\mu m$ ), the variation of uniaxial in-plane tensile strain along the out-of-plane direction (c-axis) is negligible. The nanoflakes were intentionally oriented when they were transferred onto the SiO<sub>2</sub>/Si substrate so that a uniaxial strain can be applied along either the a-axis or the b-axis. The two representative devices discussed in the main paper are labeled as device A (thickness of nanoflake 26 nm) and device B (thickness of nanoflake 54 nm), with the strain being applied parallel to the a and b axes, respectively. The crystallographic orientations of the nanoflakes were confirmed using polarized Raman spectroscopy, as described in the Supporting Information (Section 2).

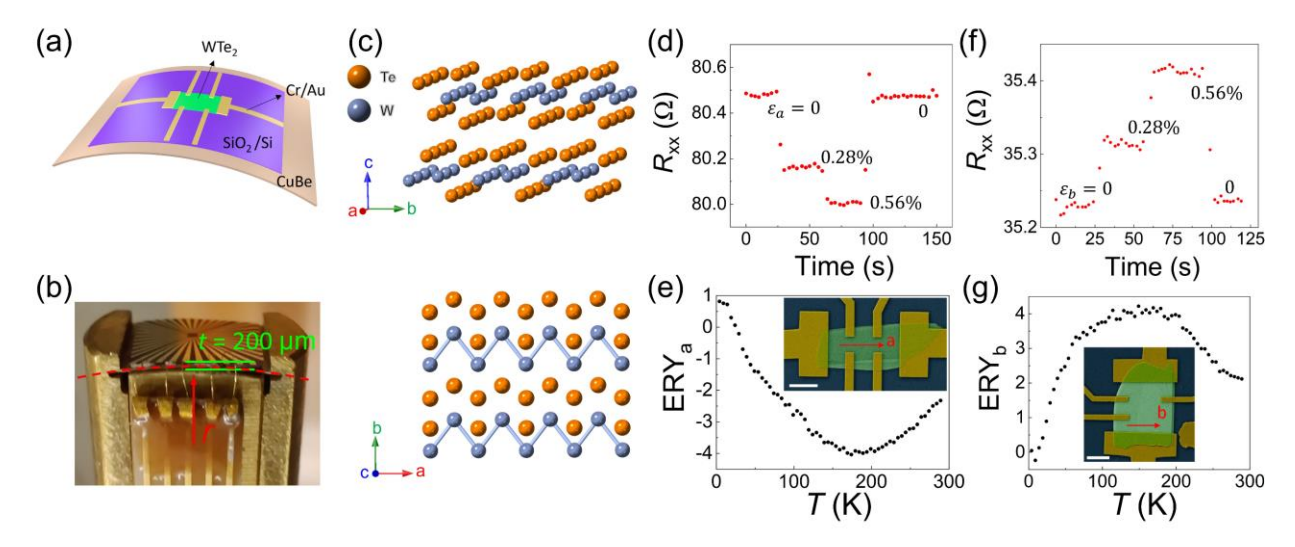


**Figure 1.** (a) Schematic of the flexible nanodevice illustrating a bent WTe<sub>2</sub> nanoplate on SiO<sub>2</sub>/Si substrate and beryllium copper sheet. (b) Photograph of a bent device. The curvature is illustrated by the red dashed line, and the radius of curvature r (not drawn to scale) is derived by measuring the pushed distance from its flat, neutral state. (Figure S1) (c) Upper panel: layered crystal structure of WTe<sub>2</sub>. Lower panel: top view of WTe<sub>2</sub> monolayer. The W atomic chain along the a axis results in strong electronic anisotropy. Chemical bonds are drawn only for illustrative purpose. (d), (e) and (f), (g) are the response of the four-terminal longitudinal resistance to strain at 290 K and elastoresistivity of device A and device B, in which strain is applied along a and b axes respectively. We take the Poisson ratio v = 0.16 to subtract the geometric effect in (e) and (g), as

detailed in the Supporting Information (Section 3). The insets in (e) and (g) are representative false-colored SEM images of the two types of devices. Both scale bars are 5 µm.

We first studied the effect of strain on the four-terminal resistance at 290 K. As shown in Figure 1d,f, a tensile strain of  $\varepsilon_a$ =0.28% (or 0.56%) along the a-axis results in a decrease of ~0.4% (or 0.6%) in the resistance, whereas the resistance is increased by ~0.2% (or 0.5%) when a tensile strain of  $\varepsilon_b$ =0.28% (or 0.56%) is applied along the b axis. This observation highlights the significant anisotropy of the strain effect. It is worth noting that the minor geometric change of the nanoflake under a uniaxial strain can slightly alter its resistance, as well. As analyzed in the Supporting Information (Section 3), however, this geometric effect results in an increase (or decrease) of the measured resistance when the strain is applied along the a (or b) axis, which is opposite to our observations. Therefore, the observed change in resistance must predominantly arise from strain-induced alterations in the electronic properties, rather than a geometric effect. Furthermore, the resistance promptly returns to its original value as soon as the strain is released, indicating the absence of residual strain.

We next studied the influence of strain on the temperature-dependent (magneto-) resistivity down to 4 K. The temperature dependence without strain (Figure S4) shows a typical metallic behavior, and the resistivity values are comparable with previous reports on WTe<sub>2</sub> nanoflakes of similar thicknesses.<sup>37, 53</sup> The influence of strain is characterized by the elastoresistivity (ERY) which we define as ERY =  $\frac{(\rho_{xx}(\varepsilon) - \rho_{xx}(0))/\rho_{xx}(0)}{\varepsilon}$ , where  $\rho_{xx}(0)$  and  $\rho_{xx}(\varepsilon)$  are the four-terminal longitudinal resistivities at zero strain and at a strain of  $\varepsilon$ , respectively. In the calculation of the resistivities, we have taken into account the aforementioned geometric effect. Figure 1e,g show the temperature dependence of the ERY along the a and b axes (ERY<sub>a</sub> and ERY<sub>b</sub>) from 290 K down to 4 K. Both ERY<sub>a</sub> and ERY<sub>b</sub> exhibit a non-monotonic dependence on temperature: ERY<sub>a</sub>-T

forms a concave curve, whereas ERY<sub>b</sub>-*T* is convex. At 290 K, ERY<sub>a</sub> and ERY<sub>b</sub> take negative and positive values, respectively, consistent with the observations in Figure 1d,f. The magnitudes of ERY<sub>a</sub> and ERY<sub>b</sub> both initially increase as the temperature decreases, reaching their maxima around 170 K. Upon further cooling, their magnitudes decrease and eventually approach zero or change signs depending on the Poisson's ratio used in the calculation of geometry effect. The non-monotonic temperature dependence of ERY suggests the existence of competing effects, due to the multiple types of charge carriers with different mobilities that contribute collectively to the charge transport.

Theoretical analysis in the case of *compressive* strain<sup>26</sup> suggests that the strain has a strong impact on the charge carrier density, which is a dominant effect for the observed elastoresistance. To experimentally determine the charge carrier density, we performed MR and Hall measurements at different temperatures under the application of tensile strains. Figure 2 displays the MR and Hall resistivity at two representative temperatures of  $T=30~\mathrm{K}$  and 200 K and strains of  $\varepsilon_{a,b}=0$ and 0.56%. A full set of data is provided in the Supporting Information (Section 5). The magnetoresistance is defined as:  $MR = [\rho_{xx}(B) - \rho_{xx}(0)]/\rho_{xx}(0)$ , where  $\rho_{xx}(0)$  and  $\rho_{xx}(B)$ are the longitudinal resistivity at zero magnetic field and B, respectively. The MR without strain has a typical quadratic dependence on the magnetic field and its values are comparable with those reported in WTe<sub>2</sub> nanoflakes<sup>53-57</sup> but are orders of magnitude lower than in bulk WTe<sub>2</sub> crystals<sup>24,</sup> <sup>53, 58</sup> due to the imperfect compensation of electron and hole densities and smaller carrier mobility in nanoflakes. 53 The Hall resistivity  $\rho_{xy}$  without strain is not strictly linear as a function of magnetic field especially at low temperatures, due to the presence of both electrons and holes.<sup>59</sup> At 30 K, both  $\varepsilon_a$  and  $\varepsilon_b$  exhibit a small impact on MR and  $\rho_{xy}$ . However, their effects become more evident as the temperature increases, which may be due to the effect of the strain on the

phonon spectrum.<sup>26</sup> Specifically,  $\varepsilon_a$  increases the magnitudes of the MR and  $\rho_{xy}$ , whereas  $\varepsilon_b$  decreases the magnitudes. Potential artifacts due to thermal cycles or structural defects induced by strain such as cracks or interlayer slippage are ruled out by highly reproducible measurements after multiple cycles (Figure S7). We also note that bending the device inevitably alters the angle between the sample surface and the magnetic field, which in theory could result in a smaller effective field and decrease the MR and  $\rho_{xy}$ . Nevertheless, a quantitative analysis presented in the Supporting Information (Section 7) indicates that this effect is too small to cause any observable decrease in MR or  $\rho_{xy}$ . Therefore, the observed change of MR and  $\rho_{xy}$  in Figure 2c,d must be intrinsically induced by the applied strain.

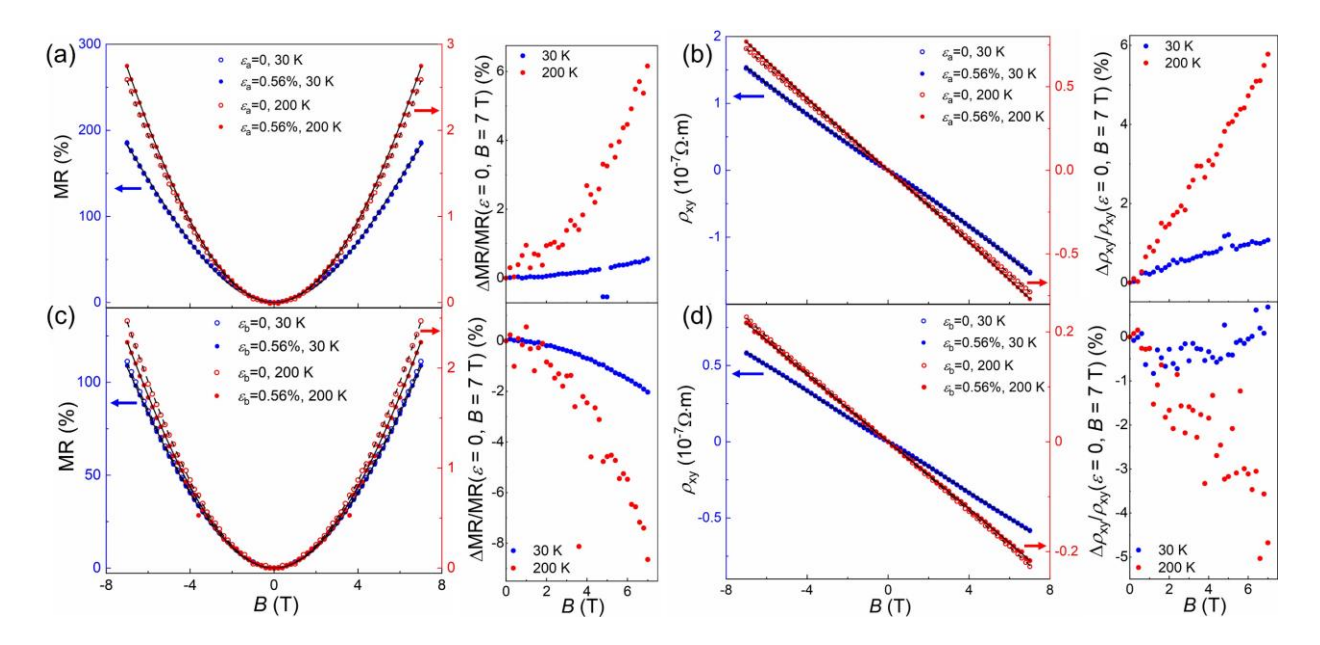


Figure 2. Magnetoresistance (a), (c) and Hall resistivity (b), (d) of device A and device B. Data in blue and red correspond to different temperatures: 30 K and 200 K. Solid and hollow circles represent 0.56% and zero strain. The magnetic field was applied perpendicular to the sample surface (i.e., along the c-axis) and was swept between -7 T and 7 T. The data at 30 K and 200 K correspond to the y-axis labels in blue and red respectively, as indicated by the arrows of the corresponding colors. Black dash line and solid line are the fitting curves for the data of zero strain and 0.56% strain respectively. The outlier due to measurement artifact in (c) was not

included for the fitting. The right panels show the strain-induced change in MR and  $\rho_{xy}$  divided by the corresponding data point with zero strain at 7 T. The device-to-device variation between device A and B may arise from the different thicknesses.

To extract the charge carrier densities, we have applied a classical two-band model that has been widely used in WTe<sub>2</sub>.<sup>37, 53, 56, 59-63</sup> The MR and  $\rho_{xy}$  are described as follows:

$$MR(B) = \frac{(n\mu_e + p\mu_h)^2 + \mu_e \mu_h (n\mu_e + p\mu_h)(p\mu_e + n\mu_h)B^2}{(n\mu_e + p\mu_h)^2 + (p - n)^2 \mu_e^2 \mu_h^2 B^2} - 1$$

$$\rho_{xy}(B) = \frac{(p\mu_h^2 - n\mu_e^2)B + \mu_e^2 \mu_h^2 (p - n)B^3}{e[(n\mu_e + p\mu_h)^2 + (p - n)^2 \mu_e^2 \mu_h^2 B^2]}$$

where n, p are the densities of the electrons and holes, respectively, and  $\mu_e$  and  $\mu_h$  are their mobilities, respectively.<sup>64,65</sup> By fitting the MR and  $\rho_{xy}$  data with the above two equations (Figure 2), we have extracted the electron and hole densities and mobilities at different strains and temperatures. Figure 3a,b depict the temperature dependence of the resulting electron and hole densities for device A and device B under zero applied strain, which are consistent with previous studies of thin flakes.<sup>37,62,63</sup>

The electron density n shows an anisotropic dependence on the strain, in which it increases as tensile strain is applied along the a-axis and decreases along the b-axis. For example, as shown in Figure 3c,d, the electron density decreases by 3% when applying  $\varepsilon_a$ =0.56% at 150 K and increases by 7% when applying  $\varepsilon_b$ =0.56% at 150 K. The tensile strain has a qualitatively similar influence on the hole density p at low temperatures, where the p decreases under an a-axis strain but increases with a b-axis strain (Figure S9a,d). This strain-dependence of charge carrier density is surprising as an a-axis (b-axis) strain generally reduces (increases) the resistivity (Figure 1e,g). However, as seen in Figure S9b,e, the influence of charge carrier density is overwhelmed by the more

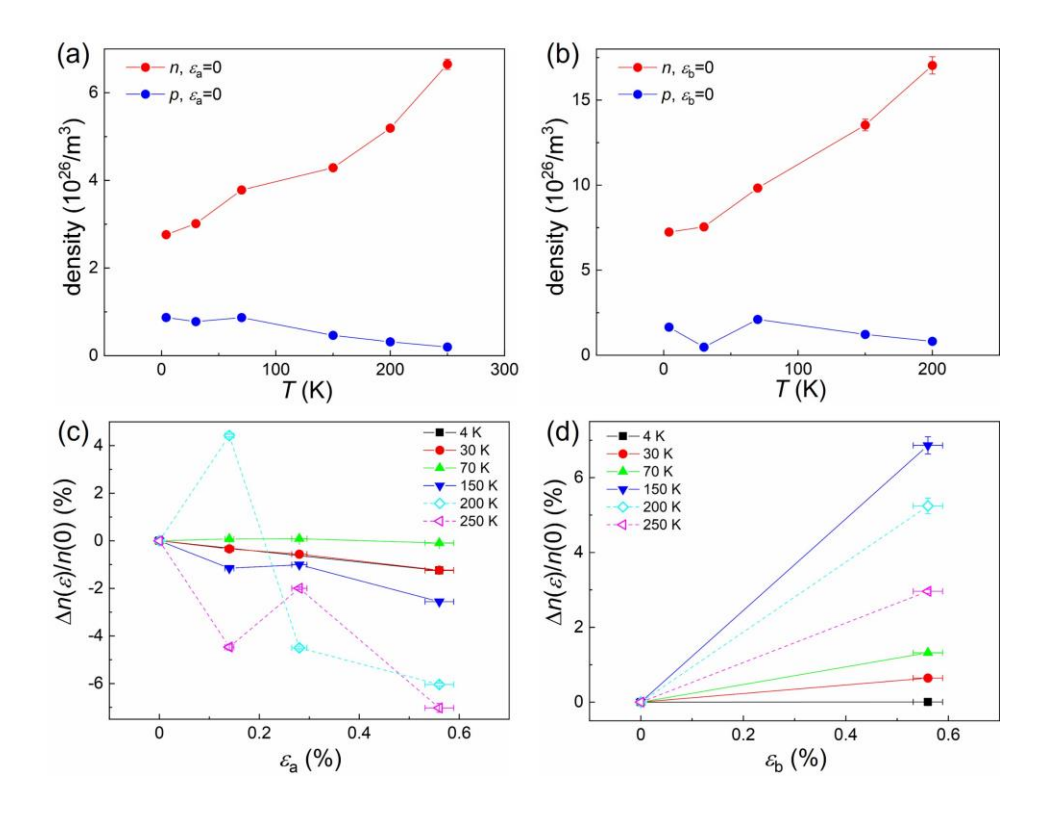
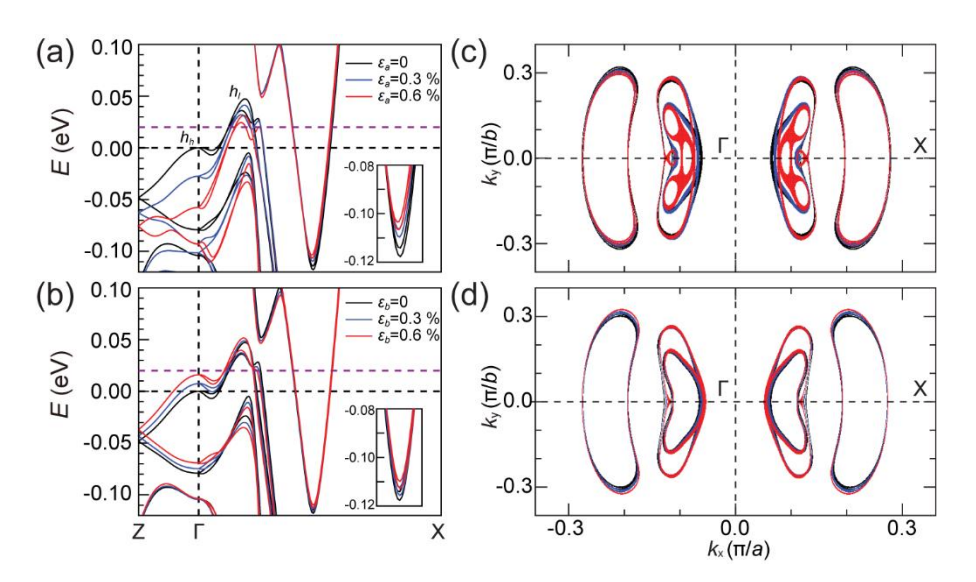


Figure 3. Electron and hole densities with zero strain as functions of temperature for (a) device A and (b) device B. The relative change of electron density at different temperatures resulted from the application of strain along (c) a axis and (d) b axis, where  $\Delta n = n(\varepsilon) - n(0)$ . The scattered data above 150 K (dashed lines with open symbols) are attributed to the breakdown of the two-band model. The error bars for the carrier densities are from the fitting and for the strains are from the error propagation of the estimated measurement uncertainties. Given the nearly monotonic strain dependence at low temperatures, only zero and 0.56% strain were applied for device B to collect the magneto-transport data.

pronounced change of electron mobility  $\mu_e$  with strain, which increases under an a-axis strain and decreases with a b-axis strain. The increase of mobility is consistent with the recent study of bulk WTe<sub>2</sub> crystal where a compressive strain along the a-axis increases the effective mass of electron and possibly the scattering rate as well at low temperatures.<sup>26</sup> Additionally, uniaxial tensile strain has also shown to enhance the electron mobility in another 2D material MoS<sub>2</sub>.<sup>21, 22</sup> Although the strain dependence of  $\mu_h$  is less clear (Figure S9c,f), we note that the dominant influence is from

the electrons as n is about three times as large as p in our nanoflakes. The strain dependent data become more scattered above 150 K. In addition to the reduced signal-to-noise ratio of the MR and  $\rho_{xy}$  at high temperatures, we also attribute this to the breakdown of the two-band model. As will be presented in the band structure calculations below, a third heavy hole band coexists with the light hole band, and the contribution to transport from the heavy holes becomes more prominent as the temperature increases.



**Figure 4.** Calculated band structures of WTe<sub>2</sub> without strain (black), and with strains of  $\varepsilon$ =0.3% (blue) and  $\varepsilon$ =0.6% (red). Strains applied along (a) a-axis and (b) b-axis, with insets showing enlarged electronic pocket structures. The  $h_h$  and  $h_l$  represent the heavy and light hole band, respectively. The Fermi level is set at zero, with an additional chemical potential shift set at 0.02 eV, indicated in purple line. Fermi surfaces at  $k_z$ =0 are illustrated at a chemical potential of 0.02 eV in (c) and (d), corresponding to the strain conditions described in (a) and (b), respectively. Line colors represent identical strain levels as in (a) and (b).

DFT calculations of the electronic band structures were carried out without and with tensile strains (0.3% and 0.6%) along the a- and b- axes. Figure 4a,b show the band structures along the high symmetry lines ( $Z - \Gamma$  and  $\Gamma - X$ ). In the absence of strain, a doubly degenerate electron pocket and a pair of light hole pockets cross the intrinsic Fermi level (i.e., E = 0 meV) along the

 $\Gamma - X$  direction, revealing the semimetallic nature of the system. The hole bands near the  $\Gamma$  point are rather flat and are understood as the heavy hole bands with a large effective mass<sup>24, 32, 33, 37, 66-70</sup>. It is worth noting that the chemical potential determined experimentally by angle-resolved photoemission spectroscopy studies in real samples is typically a few tens of meV above the intrinsic Fermi level.<sup>33</sup> This n-type doped nature is possibly due to the presence of intrinsic point defects in the samples. Given that the electron density is about three times as high as the hole density in our devices, we estimate the chemical potential in our case to be at ~20 meV (purple dashed line in Figure 4a,b).

Tensile strain applied along the a-axis moves the multiple hole bands downwards and the electron bands (below the chemical potential) slightly upwards, whereas the same tensile strain in the b-axis shifts both the hole bands and the electron bands upwards. Following Refs.27, 28, this anisotropic strain effect can be understood based on the orbitally decomposed band structure near the  $\Gamma$  point. As shown in Figure S10, both the heavy hole and light hole pockets are mainly composed of  $p_x$  and  $d_{xz}$  orbitals. Taking  $p_x$  as an example, antibonding states will be formed along the x (same as the a) axis between  $p_x$  orbitals of adjacent Te atoms, which tends to lift the band energy. When tensile strain is applied along this axis, the distance along it between adjacent Te atoms increases, the energy cost of antibonding becomes smaller, and a decrease in the band energy results. This is consistent with the fact that the hole bands are shifted downward in Figure 4a. By contrast, bonding states form along the y (same as the b) axis, so that the energy of the hole bands increases when tensile strain is applied along it [Figure 4b]. A similar analysis can be applied to the  $d_{xz}$  orbitals and results in the same behavior. On the other hand, the electron pocket is composed of a  $p_z$  orbital and multiple d orbitals  $(d_{xy}, d_{x^2-y^2}, d_{z^2})$ . Bonding is formed along both the x and y axes if we only consider the  $p_z$  orbital, so that the band energy will be increased when tensile

strain is applied along either of them, which is seen in Figures 4a and b. However, the multiple d orbitals form both bonding and antibonding along both the a and b axes, so that the overall strain effect involves a competition among them. This makes qualitative analysis very challenging. Given the relatively large weight of  $p_z$  in the orbital projections, and the strain effect exhibited by the electron pocket [Figures 4a and b], we believe the  $p_z$  orbital is dominant in this analysis. Furthermore, it indeed explains why the electron pocket is less sensitive to strain than the hole pockets, as the two orbitals within the hole pockets have the same behavior under strain, leading to a collectively stronger response.

Although the shift of the electron bands by strain appears to be minimal along the  $\Gamma - X$  direction, the Fermi surface of the electron pockets is notably changed by strain. As shown in Figure 4c, the electron pockets have clearly shrunk with no change to their topology when a tensile strain is applied along the a-axis, corresponding to a decrease in electron density. In the case of b-axis strain, the electron pockets have shrunk slightly in the  $k_x$  direction, consistent with the upward shift of bands in the  $\Gamma - X$  direction, but are expanded more dramatically in the  $k_y$  direction, resulting in an overall increase of Fermi surface area and electron density. The change of Fermi surface area is monotonic as a function of strain (Figure 4c,d) and is consistent with the experimentally observed strain-dependence of the electron density at least at low temperatures (Figure 3c,d).

On the other hand, the influence of strain on the hole bands/pockets is more complex due to the coexistence of light holes and heavy holes. Although the heavy hole bands are below the chemical potential, they could still play an essential role in the electrical transport at high temperatures.<sup>26</sup> When a tensile strain is applied in the *a*-axis, the heavy hole bands exhibit a more pronounced downward shift than the light hole bands (Figure 4a), suggesting that the contribution

of the heavy hole bands to the electrical transport is significantly suppressed. As the light hole bands move downwards by strain, the Fermi surface shows a complicated evolution. In particular, the light hole pockets undergo transitions in which small pockets are pinched off, so that the topology of the Fermi surface becomes more complicated. Nevertheless, the total volume enclosed by the Fermi surface decreases, corresponding to an overall decrease of hole density at low temperatures. When strain is applied along the *b*-axis, the heavy hole bands are clearly moved upwards whereas the shift of the light hole bands appears to be minimal. Therefore, it is expected that the contribution of the heavy holes to the transport at high temperature is slightly enhanced with the *b*-axis strain, which seems consistent with the breakdown of the two-band model (or the more scattered strain dependence of carrier density and mobility) at a lower temperature than in the case of *a*-axis strain. Due to the minimal change of light hole bands, the Fermi surface area of the hole pockets increases marginally as shown in Figure 4d.

To quantify the influence of strain, we calculated the electron and hole densities with and without strain at different chemical potentials, ranging from 0 eV to 0.05 eV. This range was chosen to cover the experimental values that have been reported in different samples and at different temperatures in the literature.<sup>33</sup> As shown in Figure 5, the electron density decreases (increases) when a tensile strain is applied along the a-axis (b-axis), and this change is nearly independent of the chemical potential. As briefly mentioned earlier, the strain induced change in electron density is mainly attributed to the change of Fermi surface in the  $k_y$  direction. Quantitatively, this change is essentially the same over a range of chemical potentials. As noted above, the change largely occurs due to a sensitivity of the Fermi surface along the  $k_y$  direction to strain: the width decreases (increases) with tensile strain along the a (b) axis. This behavior persists over the range of chemical potentials we examined in our calculations.

The behavior of the hole density is again notably more complex due to the presence of multiple hole bands/pockets. In the absence of strain, the hole density decreases with the increase of chemical potential as expected. A notable characteristic is the abrupt decrease in hole density near  $\sim 0.03$  eV, which is attributed to the disappearance of the hole pocket in the lower energy region of the degenerated light hole band.<sup>59</sup> When a tensile strain is applied along the *a*-axis, the overall hole bands shift downwards, which not only reduces the hole density but also causes an abrupt decrease to occur at a lower chemical potential. Conversely, applying strain along the *b*-axis results in an increase of hole density in the low chemical potential region (<0.01 eV), due to the upward shift of the heavy hole bands which eventually cross the chemical potential. The hole density, however, is nearly independent of the strain at higher chemical potentials as the main contribution is from the light hole bands which are almost unchanged by strain.

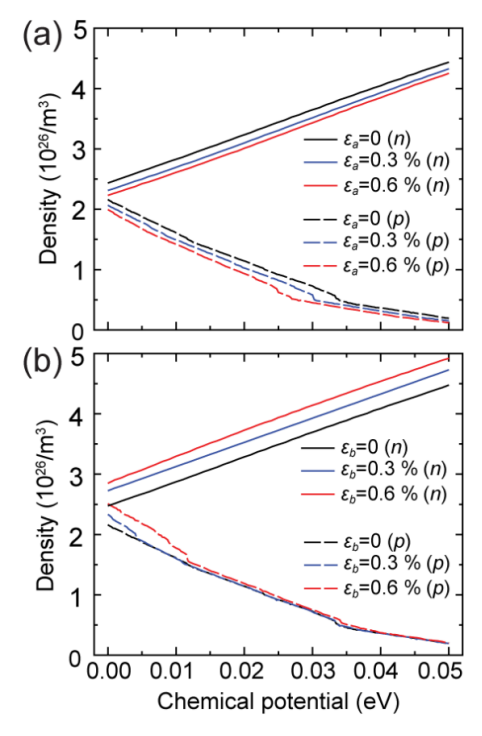


**Figure 5.** Calculated electron and hole densities as functions of chemical potential with a tensile strain applied along (a) a-axis and (b) b-axis. The solid line represents electron densities, while the dashed line indicates hole densities. Black, blue, and red colors correspond to the  $\varepsilon$ =0, 0.3%,

and 0.6%, respectively.

#### 4. Conclusions

In summary, we report for the first-time strain dependent magneto-transport measurements on vdW thin layers at low temperatures. By applying a uniaxial tensile strain along two in-plane crystallographic axes, we observed a clear anisotropic effect in the semimetal WTe<sub>2</sub>, where its resistance has opposite responses to the applied strain in the two directions, e.g., it decreases as a tensile strain is applied along the *a*-axis whereas increases when the same strain is in the *b*-axis. The electron density extracted from the magnetoresistance and Hall measurements decreases as a function of tensile strain along the *a*-axis and increases with an *b*-axis strain. The anisotropic strain-dependence of electron and hole densities is well understood by density functional theory calculations of electronic band structures and Fermi surfaces. Our work experimentally demonstrates strain engineering as an effective tool to tune the electronic transport properties of vdW semimetals, thereby broadening the application scope of both strain engineering and vdW semimetals.

### ASSOCIATED CONTENT

**Supporting Information**: Experimental and calculation details, strain calculation, polarized Raman spectroscopy, estimation and subtraction of the geometric effect, temperature-dependent resistivity measurements, full data of magnetoresistance and Hall resistivity measurements, change of the effective magnetic field caused by bending, reproduced magneto-transport measurements, dependence of the hole density and carrier mobilities on strain.

The following files are available free of charge.

Supporting Information (file type, i.e., PDF)

**AUTHOR INFORMATION** 

**Corresponding Author** 

Shixiong Zhang - Department of Physics, Indiana University, Bloomington, Indiana 47405, United

States; Quantum Science and Engineering Center, Indiana University, Bloomington, Indiana

47405, United States

Email: sxzhang@indiana.edu

**Author Contributions** 

T.X. Zhang and J.H. Hong contributed equally. The manuscript was written through contributions

of all authors. All authors have given approval to the final version of the manuscript.

Notes

The authors declare no competing financial interest.

ACKNOWLEDGMENT

We acknowledge support from the U.S. National Science Foundation through grant nos. ECCS-

1936406 and DMR-1914451. C.N. and R.H. acknowledge the support by NSF Grant No. DMR-

2300640. We thank the Indiana University-Bloomington Nanoscale Characterization Facility for

access to the characterization and device fabrication tools and IU Physics Machine Shop for

instrumental assistance. We also thank Z.L. Pan for experimental assistance and D. Sprinkle for

technical assistance. This research was supported in part by Lilly Endowment, Inc., through its

support for the Indiana University Pervasive Technology Institute.

19

# References

- (1) Lee, M. L.; Fitzgerald, E. A.; Bulsara, M. T.; Currie, M. T.; Lochtefeld, A. Strained Si, SiGe, and Ge channels for high-mobility metal-oxide-semiconductor field-effect transistors. *Journal of Applied Physics* **2004**, *97* (1), 011101.
- (2) Hicks, C. W.; Brodsky, D. O.; Yelland, E. A.; Gibbs, A. S.; Bruin, J. A. N.; Barber, M. E.; Edkins, S. D.; Nishimura, K.; Yonezawa, S.; Maeno, Y.; Mackenzie, A. P. Strong Increase of Tc of Sr<sub>2</sub>RuO<sub>4</sub> Under Both Tensile and Compressive Strain. *Science* **2014**, *344* (6181), 283-285.
- (3) Park, J.; Sakai, H.; Mackenzie, A. P.; Hicks, C. W. Effect of uniaxial stress on the magnetic phases of CeAuSb<sub>2</sub>. *Physical Review B* **2018**, *98* (2), 024426.
- (4) Hosoi, S.; Tachibana, F.; Sakaguchi, M.; Ishida, K.; Shimozawa, M.; Izawa, K.; Fuseya, Y.; Kinoshita, Y.; Tokunaga, M. Highly strain-tunable charge valley transport in bismuth. *arXiv* preprint arXiv:2309.05285 **2023**.
- (5) Chu, J.-H.; Kuo, H.-H.; Analytis, J. G.; Fisher, I. R. Divergent nematic susceptibility in an iron arsenide superconductor. *Science* **2012**, *337* (6095), 710-712.
- (6) Riggs, S. C.; Shapiro, M.; Maharaj, A. V.; Raghu, S.; Bauer, E.; Baumbach, R.; Giraldo-Gallo, P.; Wartenbe, M.; Fisher, I. Evidence for a nematic component to the hidden-order parameter in URu<sub>2</sub>Si<sub>2</sub> from differential elastoresistance measurements. *Nature Communications* 2015, 6 (1), 6425.
- (7) Rosenberg, E. W.; Chu, J.-H.; Ruff, J. P.; Hristov, A. T.; Fisher, I. R. Divergence of the quadrupole-strain susceptibility of the electronic nematic system YbRu<sub>2</sub>Ge<sub>2</sub>. *Proceedings of the National Academy of Sciences* **2019**, *116* (15), 7232-7237.
- (8) Akinwande, D.; Petrone, N.; Hone, J. Two-dimensional flexible nanoelectronics. *Nature Communications* **2014**, *5* (1), 5678.
- (9) Roldán, R.; Castellanos-Gomez, A.; Cappelluti, E.; Guinea, F. Strain engineering in semiconducting two-dimensional crystals. *Journal of Physics: Condensed Matter* **2015**, *27* (31), 313201.
- (10) Si, C.; Sun, Z.; Liu, F. Strain engineering of graphene: a review. *Nanoscale* **2016**, *8* (6), 3207-3217.
- (11) Manzeli, S.; Ovchinnikov, D.; Pasquier, D.; Yazyev, O. V.; Kis, A. 2D transition metal dichalcogenides. *Nature Reviews Materials* **2017**, *2* (8), 17033.

- (12) Dai, Z.; Liu, L.; Zhang, Z. Strain Engineering of 2D Materials: Issues and Opportunities at the Interface. *Advanced Materials* **2019**, *31* (45), 1805417.
- (13) Peng, Z.; Chen, X.; Fan, Y.; Srolovitz, D. J.; Lei, D. Strain engineering of 2D semiconductors and graphene: from strain fields to band-structure tuning and photonic applications. *Light: Science & Applications* **2020**, *9* (1), 190.
- (14) Song, W.; Yang, L. Quasiparticle band gaps and optical spectra of strained monolayer transition-metal dichalcogenides. *Physical Review B* **2017**, *96* (23), 235441.
- (15) Fei, R.; Yang, L. Strain-Engineering the Anisotropic Electrical Conductance of Few-Layer Black Phosphorus. *Nano Letters* **2014**, *14* (5), 2884-2889.
- (16) Conley, H. J.; Wang, B.; Ziegler, J. I.; Haglund, R. F., Jr.; Pantelides, S. T.; Bolotin, K. I. Bandgap Engineering of Strained Monolayer and Bilayer MoS<sub>2</sub>. *Nano Letters* **2013**, *13* (8), 3626-3630.
- (17) He, K.; Poole, C.; Mak, K. F.; Shan, J. Experimental Demonstration of Continuous Electronic Structure Tuning via Strain in Atomically Thin MoS<sub>2</sub>. *Nano Letters* **2013**, *13* (6), 2931-2936.
- (18) Desai, S. B.; Seol, G.; Kang, J. S.; Fang, H.; Battaglia, C.; Kapadia, R.; Ager, J. W.; Guo, J.; Javey, A. Strain-Induced Indirect to Direct Bandgap Transition in Multilayer WSe<sub>2</sub>. *Nano Letters* **2014**, *14* (8), 4592-4597.
- (19) Wang, Y.; Cong, C.; Yang, W.; Shang, J.; Peimyoo, N.; Chen, Y.; Kang, J.; Wang, J.; Huang, W.; Yu, T. Strain-induced direct-indirect bandgap transition and phonon modulation in monolayer WS<sub>2</sub>. *Nano Research* **2015**, *8* (8), 2562-2572.
- (20) Aslan, B.; Datye, I. M.; Mleczko, M. J.; Sze Cheung, K.; Krylyuk, S.; Bruma, A.; Kalish, I.; Davydov, A. V.; Pop, E.; Heinz, T. F. Probing the Optical Properties and Strain-Tuning of Ultrathin Mo<sub>1-x</sub>W<sub>x</sub>Te<sub>2</sub>. *Nano Letters* **2018**, *18* (4), 2485-2491.
- (21) Datye, I. M.; Daus, A.; Grady, R. W.; Brenner, K.; Vaziri, S.; Pop, E. Strain-Enhanced Mobility of Monolayer MoS<sub>2</sub>. *Nano Letters* **2022**, *22* (20), 8052-8059.
- (22) Chen, Y.; Lu, D.; Kong, L.; Tao, Q.; Ma, L.; Liu, L.; Lu, Z.; Li, Z.; Wu, R.; Duan, X.; Liao, L.; Liu, Y. Mobility Enhancement of Strained MoS<sub>2</sub> Transistor on Flat Substrate. *ACS Nano* **2023**, *17* (15), 14954-14962.
- (23) Cenker, J.; Sivakumar, S.; Xie, K.; Miller, A.; Thijssen, P.; Liu, Z.; Dismukes, A.; Fonseca, J.; Anderson, E.; Zhu, X.; Roy, X.; Xiao, D.; Chu, J.-H.; Cao, T.; Xu, X. Reversible strain-induced magnetic phase transition in a van der Waals magnet. *Nature Nanotechnology* **2022**,

- 17 (3), 256-261.
- (24) Ali, M. N.; Xiong, J.; Flynn, S.; Tao, J.; Gibson, Q. D.; Schoop, L. M.; Liang, T.; Haldolaarachchige, N.; Hirschberger, M.; Ong, N. P.; Cava, R. J. Large, non-saturating magnetoresistance in WTe<sub>2</sub>. *Nature* **2014**, *514* (7521), 205-208.
- (25) Eftekhari, A. Tungsten dichalcogenides (WS<sub>2</sub>, WSe<sub>2</sub>, and WTe<sub>2</sub>): materials chemistry and applications. *Journal of Materials Chemistry A* **2017**, *5* (35), 18299-18325.
- (26) Jo, N. H.; Wang, L.-L.; Orth, P. P.; Bud'ko, S. L.; Canfield, P. C. Magnetoelastoresistance in WTe<sub>2</sub>: Exploring electronic structure and extremely large magnetoresistance under strain. *Proceedings of the National Academy of Sciences* **2019**, *116* (51), 25524-25529.
- (27) Zhao, C.; Hu, M.; Qin, J.; Xia, B.; Liu, C.; Wang, S.; Guan, D.; Li, Y.; Zheng, H.; Liu, J.; Jia, J. Strain Tunable Semimetal--Topological-Insulator Transition in Monolayer 1T'-WTe<sub>2</sub>. *Physical Review Letters* **2020**, *125* (4), 046801.
- (28) Hu, M.; Ma, G.; Wan, C. Y.; Liu, J. Realistic tight-binding model for monolayer transition metal dichalcogenides of 1T' structure. *Physical Review B* **2021**, *104* (3), 035156.
- (29) Amin, B.; Kaloni, T. P.; Schwingenschlögl, U. Strain engineering of WS<sub>2</sub>, WSe<sub>2</sub>, and WTe<sub>2</sub>. *Rsc Advances* **2014**, *4* (65), 34561-34565.
- (30) Xiang, H.; Xu, B.; Liu, J.; Xia, Y.; Lu, H.; Yin, J.; Liu, Z. Quantum spin Hall insulator phase in monolayer WTe<sub>2</sub> by uniaxial strain. *AIP Advances* **2016**, *6* (9), 095005.
- (31) Torun, E.; Sahin, H.; Cahangirov, S.; Rubio, A.; Peeters, F. M. Anisotropic electronic, mechanical, and optical properties of monolayer WTe<sub>2</sub>. *Journal of Applied Physics* **2016**, *119* (7), 074307.
- (32) Pletikosić, I.; Ali, M. N.; Fedorov, A. V.; Cava, R. J.; Valla, T. Electronic Structure Basis for the Extraordinary Magnetoresistance in WTe<sub>2</sub>. *Physical Review Letters* **2014**, *113* (21), 216601.
- (33) Wu, Y.; Jo, N. H.; Ochi, M.; Huang, L.; Mou, D.; Bud'ko, S. L.; Canfield, P. C.; Trivedi, N.; Arita, R.; Kaminski, A. Temperature-Induced Lifshitz Transition in WTe<sub>2</sub>. *Physical Review Letters* **2015**, *115* (16), 166602.
- (34) Thoutam, L. R.; Wang, Y. L.; Xiao, Z. L.; Das, S.; Luican-Mayer, A.; Divan, R.; Crabtree, G. W.; Kwok, W. K. Temperature-Dependent Three-Dimensional Anisotropy of the Magnetoresistance in WTe<sub>2</sub>. *Physical Review Letters* 2015, 115 (4), 046602.
- (35) Zhao, Y.; Liu, H.; Yan, J.; An, W.; Liu, J.; Zhang, X.; Wang, H.; Liu, Y.; Jiang, H.; Li, Q.;

- Wang, Y.; Li, X.-Z.; Mandrus, D.; Xie, X. C.; Pan, M.; Wang, J. Anisotropic magnetotransport and exotic longitudinal linear magnetoresistance in WTe<sub>2</sub> crystals. *Physical Review B* **2015**, *92* (4), 041104.
- (36) Wang, Y.; Liu, E.; Liu, H.; Pan, Y.; Zhang, L.; Zeng, J.; Fu, Y.; Wang, M.; Xu, K.; Huang, Z.; Wang, Z.; Lu, H.-Z.; Xing, D.; Wang, B.; Wan, X.; Miao, F. Gate-tunable negative longitudinal magnetoresistance in the predicted type-II Weyl semimetal WTe<sub>2</sub>. *Nature Communications* **2016**, *7* (1), 13142.
- (37) He, P.; Hsu, C.-H.; Shi, S.; Cai, K.; Wang, J.; Wang, Q.; Eda, G.; Lin, H.; Pereira, V. M.; Yang, H. Nonlinear magnetotransport shaped by Fermi surface topology and convexity. *Nature Communications* **2019**, *10* (1), 1290.
- (38) Tan, C.; Deng, M.-X.; Zheng, G.; Xiang, F.; Albarakati, S.; Algarni, M.; Farrar, L.; Alzahrani, S.; Partridge, J.; Yi, J. B.; Hamilton, A. R.; Wang, R.-Q.; Wang, L. Spin-Momentum Locking Induced Anisotropic Magnetoresistance in Monolayer WTe<sub>2</sub>. *Nano Letters* **2021**, *21* (21), 9005-9011.
- (39) Lee, C.; Wei, X.; Kysar, J. W.; Hone, J. Measurement of the Elastic Properties and Intrinsic Strength of Monolayer Graphene. *Science* **2008**, *321* (5887), 385-388.
- (40) Castellanos-Gomez, A.; Poot, M.; Steele, G. A.; van der Zant, H. S. J.; Agraït, N.; Rubio-Bollinger, G. Elastic Properties of Freely Suspended MoS<sub>2</sub> Nanosheets. *Advanced Materials* **2012**, *24* (6), 772-775.
- (41) Huang, M.; Yan, H.; Heinz, T. F.; Hone, J. Probing Strain-Induced Electronic Structure Change in Graphene by Raman Spectroscopy. *Nano Letters* **2010**, *10* (10), 4074-4079.
- (42) Yang, W.; Coughlin, A. L.; Webster, L.; Ye, G.; Lopez, K.; Fertig, H. A.; He, R.; Yan, J.-A.; Zhang, S. Highly tunable Raman scattering and transport in layered magnetic Cr<sub>2</sub>S<sub>3</sub> nanoplates grown by sulfurization. *2D Materials* **2019**, *6* (3), 035029.
- (43) Coughlin, A. L.; Pan, Z.; Hong, J.; Zhang, T.; Zhan, X.; Wu, W.; Xie, D.; Tong, T.; Ruch, T.; Heremans, J. J.; Bao, J.; Fertig, H. A.; Wang, J.; Kim, J.; Zhu, H.; Li, D.; Zhang, S. Enhanced Electron Correlation and Significantly Suppressed Thermal Conductivity in Dirac Nodal-Line Metal Nanowires by Chemical Doping. *Advanced Science* **2023**, *10* (2), 2204424.
- (44) Blöchl, P. E. Projector augmented-wave method. *Physical Review B* **1994**, *50* (24), 17953-17979.
- (45) Kresse, G.; Joubert, D. From ultrasoft pseudopotentials to the projector augmented-wave

- method. Physical Review B 1999, 59 (3), 1758-1775.
- (46) Kresse, G.; Furthmüller, J. Efficient iterative schemes for ab initio total-energy calculations using a plane-wave basis set. *Physical Review B* **1996**, *54* (16), 11169-11186.
- (47) Mostofi, A. A.; Yates, J. R.; Pizzi, G.; Lee, Y.-S.; Souza, I.; Vanderbilt, D.; Marzari, N. An updated version of wannier90: A tool for obtaining maximally-localised Wannier functions. *Computer Physics Communications* **2014**, *185* (8), 2309-2310.
- (48) Nagai, Y.; Toyama, T.; Tang, Z.; Inoue, K.; Chiba, T.; Hasegawa, M.; Hirosawa, S.; Sato, T. Interactions between Fermi surfaces and Brillouin zone boundaries and phase stability of embedded metallic nanoparticles. *Physical Review B* **2009**, *79* (20), 201405.
- (49) Zhu, Z.; Lin, X.; Liu, J.; Fauqué, B.; Tao, Q.; Yang, C.; Shi, Y.; Behnia, K. Quantum Oscillations, Thermoelectric Coefficients, and the Fermi Surface of Semimetallic WTe<sub>2</sub>. *Physical Review Letters* **2015**, *114* (17), 176601.
- (50) Brown, B. E. The crystal structures of WTe<sub>2</sub> and high-temperature MoTe<sub>2</sub>. *Acta Crystallographica* **1966**, *20* (2), 268-274.
- (51) Atkin, J. M.; Berweger, S.; Chavez, E. K.; Raschke, M. B.; Cao, J.; Fan, W.; Wu, J. Strain and temperature dependence of the insulating phases of VO<sub>2</sub> near the metal-insulator transition. *Physical Review B* **2012**, *85* (2), 020101.
- (52) Mohiuddin, T. M. G.; Lombardo, A.; Nair, R. R.; Bonetti, A.; Savini, G.; Jalil, R.; Bonini, N.; Basko, D. M.; Galiotis, C.; Marzari, N.; Novoselov, K. S.; Geim, A. K.; Ferrari, A. C. Uniaxial strain in graphene by Raman spectroscopy: G peak splitting, Gruneisen parameters, and sample orientation. *Physical Review B* **2009**, *79* (20), 205433.
- (53) Wang, L.; Gutiérrez-Lezama, I.; Barreteau, C.; Ubrig, N.; Giannini, E.; Morpurgo, A. F. Tuning magnetotransport in a compensated semimetal at the atomic scale. *Nature Communications* **2015**, *6* (1), 8892.
- (54) Luo, X.; Fang, C.; Wan, C.; Cai, J.; Liu, Y.; Han, X.; Lu, Z.; Shi, W.; Xiong, R.; Zeng, Z. Magnetoresistance and Hall resistivity of semimetal WTe<sub>2</sub> ultrathin flakes. *Nanotechnology* **2017**, *28* (14), 145704.
- (55) Woods, J. M.; Shen, J.; Kumaravadivel, P.; Pang, Y.; Xie, Y.; Pan, G. A.; Li, M.; Altman, E.
  I.; Lu, L.; Cha, J. J. Suppression of Magnetoresistance in Thin WTe<sub>2</sub> Flakes by Surface Oxidation. ACS Applied Materials & Interfaces 2017, 9 (27), 23175-23180.
- (56) Wang, Y.; Wang, L.; Liu, X.; Wu, H.; Wang, P.; Yan, D.; Cheng, B.; Shi, Y.; Watanabe, K.;

- Taniguchi, T.; Liang, S.-J.; Miao, F. Direct Evidence for Charge Compensation-Induced Large Magnetoresistance in Thin WTe<sub>2</sub>. *Nano Letters* **2019**, *19* (6), 3969-3975.
- (57) Kang, K.; Li, T.; Sohn, E.; Shan, J.; Mak, K. F. Nonlinear anomalous Hall effect in few-layer WTe<sub>2</sub>. *Nature Materials* **2019**, *18* (4), 324-328.
- (58) Wu, Y.; Jo, N. H.; Mou, D.; Huang, L.; Bud'ko, S. L.; Canfield, P. C.; Kaminski, A. Three-dimensionality of the bulk electronic structure in WTe<sub>2</sub>. *Physical Review B* **2017**, *95* (19), 195138.
- (59) Luo, Y.; Li, H.; Dai, Y. M.; Miao, H.; Shi, Y. G.; Ding, H.; Taylor, A. J.; Yarotski, D. A.; Prasankumar, R. P.; Thompson, J. D. Hall effect in the extremely large magnetoresistance semimetal WTe<sub>2</sub>. *Applied Physics Letters* **2015**, *107* (18), 182411.
- (60) Na, J.; Hoyer, A.; Schoop, L.; Weber, D.; Lotsch, B. V.; Burghard, M.; Kern, K. Tuning the magnetoresistance of ultrathin WTe<sub>2</sub> sheets by electrostatic gating. *Nanoscale* **2016**, *8* (44), 18703-18709.
- (61) Liu, W. L.; Chen, M. L.; Li, X. X.; Dubey, S.; Xiong, T.; Dai, Z. M.; Yin, J.; Guo, W. L.; Ma, J. L.; Chen, Y. N.; Tan, J.; Li, D.; Wang, Z. H.; Li, W.; Bouchiat, V.; Sun, D. M.; Han, Z.; Zhang, Z. D. Effect of aging-induced disorder on the quantum transport properties of few-layer WTe<sub>2</sub>. 2D Materials 2017, 4 (1), 011011.
- (62) Yi, Y.; Wu, C.; Wang, H.; Liu, H.; Li, H.; Zhang, H.; He, H.; Wang, J. Thickness dependent magneto transport properties of WTe<sub>2</sub> thin films. *Solid State Communications* **2017**, *260*, 45-49.
- (63) Zhang, X.; Kakani, V.; Woods, J. M.; Cha, J. J.; Shi, X. Thickness dependence of magnetotransport properties of tungsten ditelluride. *Physical Review B* **2021**, *104* (16), 165126.
- (64) Sondheimer, E. H.; Wilson, A. H. The theory of the magneto-resistance effects in metals. *Proceedings of the Royal Society of London. Series A. Mathematical and Physical Sciences* **1947**, *190* (1023), 435-455.
- (65) Murzin, S. S.; Dorozhkin, S. I.; Landwehr, G.; Gossard, A. C. Effect of hole-hole scattering on the conductivity of the two-component 2D hole gas in GaAs/(AlGa)As heterostructures. *Journal of Experimental and Theoretical Physics Letters* **1998**, 67 (2), 113-119.
- (66) Jiang, J.; Tang, F.; Pan, X. C.; Liu, H. M.; Niu, X. H.; Wang, Y. X.; Xu, D. F.; Yang, H. F.; Xie, B. P.; Song, F. Q.; Dudin, P.; Kim, T. K.; Hoesch, M.; Das, P. K.; Vobornik, I.; Wan, X.

- G.; Feng, D. L. Signature of Strong Spin-Orbital Coupling in the Large Nonsaturating Magnetoresistance Material WTe<sub>2</sub>. *Physical Review Letters* **2015**, *115* (16), 166601.
- (67) Wang, C.-L.; Zhang, Y.; Huang, J.-W.; Liu, G.-D.; Liang, A.-J.; Zhang, Y.-X.; Shen, B.; Liu, J.; Hu, C.; Ding, Y.; Liu, D.-F.; Hu, Y.; He, S.-L.; Zhao, L.; Yu, L.; Hu, J.; Wei, J.; Mao, Z.-Q.; Shi, Y.-G.; Jia, X.-W.; Zhang, F.-F.; Zhang, S.-J.; Yang, F.; Wang, Z.-M.; Peng, Q.-J.; Xu, Z.-Y.; Chen, C.-T.; Zhou, X.-J. Evidence of Electron-Hole Imbalance in WTe<sub>2</sub> from High-Resolution Angle-Resolved Photoemission Spectroscopy. *Chinese Physics Letters* 2017, 34 (9), 097305.
- (68) Di Sante, D.; Das, P. K.; Bigi, C.; Ergönenc, Z.; Gürtler, N.; Krieger, J. A.; Schmitt, T.; Ali, M. N.; Rossi, G.; Thomale, R.; Franchini, C.; Picozzi, S.; Fujii, J.; Strocov, V. N.; Sangiovanni, G.; Vobornik, I.; Cava, R. J.; Panaccione, G. Three-Dimensional Electronic Structure of the Type-II Weyl Semimetal WTe<sub>2</sub>. *Physical Review Letters* 2017, 119 (2), 026403.
- (69) Soluyanov, A. A.; Gresch, D.; Wang, Z.; Wu, Q.; Troyer, M.; Dai, X.; Bernevig, B. A. Type-II Weyl semimetals. *Nature* **2015**, *527* (7579), 495-498.
- (70) Das, P. K.; Di Sante, D.; Vobornik, I.; Fujii, J.; Okuda, T.; Bruyer, E.; Gyenis, A.; Feldman, B. E.; Tao, J.; Ciancio, R.; Rossi, G.; Ali, M. N.; Picozzi, S.; Yadzani, A.; Panaccione, G.; Cava, R. J. Layer-dependent quantum cooperation of electron and hole states in the anomalous semimetal WTe<sub>2</sub>. *Nature Communications* **2016**, *7* (1), 10847.

# **Table of contents:**

A remarkable anisotropic straintronic effect is experimentally observed in topological semimetal WTe<sub>2</sub> nanoflakes, where the magneto-transport properties have opposite responses to the uniaxial tensile strain applied in the two in-plane crystallographic orientations. Density functional theory calculations reveal the contrasting evolution of electron and hole pockets under the application of strains in the two directions.

Tongxie Zhang, Jeonghoon Hong, Amanda L. Coughlin, Cynthia Nnokwe, Michael K. Hosek, Rui He, Herbert A. Fertig, Shixiong Zhang\*

# Anisotropic Straintronic Transport in Topological Semimetal Nanoflakes

